JOURNAL OF THE AMERICAN CHEMICAL SOCIETY

Subscriber access provided by READING UNIV

Article

Oxygen Vacancy Mediated Exciton Dissociation in BiOBr for Boosting Charge-carrier-involved Molecular Oxygen Activation

Hui Wang, Dingyu Yong, Shichuan Chen, Shenlong Jiang, Xiaodong
Zhang, Wei Shao, Qun Zhang, Wensheng Yan, Bicai Pan, and Yi Xie

J. Am. Chem. Soc., **Just Accepted Manuscript** • DOI: 10.1021/jacs.7b10997 • Publication Date (Web): 10 Jan 2018

Downloaded from http://pubs.acs.org on January 10, 2018

Just Accepted

"Just Accepted" manuscripts have been peer-reviewed and accepted for publication. They are posted online prior to technical editing, formatting for publication and author proofing. The American Chemical Society provides "Just Accepted" as a free service to the research community to expedite the dissemination of scientific material as soon as possible after acceptance. "Just Accepted" manuscripts appear in full in PDF format accompanied by an HTML abstract. "Just Accepted" manuscripts have been fully peer reviewed, but should not be considered the official version of record. They are accessible to all readers and citable by the Digital Object Identifier (DOI®). "Just Accepted" is an optional service offered to authors. Therefore, the "Just Accepted" Web site may not include all articles that will be published in the journal. After a manuscript is technically edited and formatted, it will be removed from the "Just Accepted" Web site and published as an ASAP article. Note that technical editing may introduce minor changes to the manuscript text and/or graphics which could affect content, and all legal disclaimers and ethical guidelines that apply to the journal pertain. ACS cannot be held responsible for errors or consequences arising from the use of information contained in these "Just Accepted" manuscripts.

ACS Publications

Journal of the American Chemical Society is published by the American Chemical Society. 1155 Sixteenth Street N.W., Washington, DC 20036

Published by American Chemical Society. Copyright © American Chemical Society. However, no copyright claim is made to original U.S. Government works, or works produced by employees of any Commonwealth realm Crown government in the course of their duties.

Oxygen Vacancy Mediated Exciton Dissociation in BiOBr for Boosting Charge-Carrier-Involved Molecular Oxygen Activation

Hui Wang,‡ Dingyu Yong,‡ Shichuan Chen, Shenlong Jiang, Xiaodong Zhang,* Wei Shao, Qun Zhang,* Wensheng Yan, Bicai Pan, and Yi Xie*

Hefei National Laboratory for Physical Science at the Microscale, CAS Center for Excellence in Nanoscience, iChEM, Synergetic Innovation Center of Quantum Information and Quantum Physics, National Synchrotron Radiation Laboratory, University of Science and Technology of China, Hefei, Anhui, 230026, P. R. China

ABSTRACT: Excitonic effects mediated by Coulomb interactions between photogenerated electrons and holes play crucial roles in photoinduced processes of semiconductors. In term of photocatalysis, however, efforts have seldom been devoted to the relevant aspects. As for the catalysts with giant excitonic effects, the co-existing, competitive exciton generation serves as a key obstacle to the yield of free charge carriers, and hence transformation of excitons into free carriers would be beneficial for optimizing the charge-carrier-involved photocatalytic processes. Herein, by taking bismuth oxybromide (BiOBr) as a prototypical model system, we demonstrate that excitons can be effectively dissociated into charge carriers with the incorporation of oxygen vacancy, leading to excellent performances in charge-carrier-involved photocatalytic reactions such as superoxide generation and selective organic syntheses under visible-light illumination. This work not only establishes an in-depth understanding of defective structures in photocatalysts, but also paves the way for excitonic regulation via defect engineering.

INTRODUCTION

For decades, semiconductor-based photocatalytic reactions, such as water splitting, water pollution treatments, and organic syntheses, have attracted tremendous attention, due to their great potential in solving energy crisis and environmental pollution.[1–4] Among the numerous efforts, researches on the behaviors of photogenerated excited species are of great significance in pursuing advanced photocatalysts.[3–7] Nevertheless, traditional viewpoints focused on free charge carriers are somehow incomprehensive, since the Coulomb interaction-mediated many-body effects have long been ignored. Once these effects are considered, neutral excitons (or bound electron–hole pairs) might be the dominant photogenerated species, and the corresponding exciton-based resonance energy transfer could even feasibly serve as an alternative photocatalytic mechanism beyond the carrier-based charge transfer.[8–10] Moreover, the strong correlations among excitons would lead to robust exciton–exciton annihilation that opens up an important nonradiative depopulation pathway of photoexcited species.[11–13] Undoubtedly, all these aspects constitute shackles for charge-carrier-involved photocatalysis. Given the competitive relationship between excitons and charge carriers in photoexcitation processes, it would be reasonable to gain considerable quantum yields of charge carriers by dissociating excitons into free electrons and holes. In this case, it would be meaningful to explore optimized strategies of exciton dissociation for boosting charge-carrier-involved photocatalytic performance.

In view of the positive role of energetic disorder on exciton dissociation, booming charge-carrier-involved photocatalytic activity would be expected in catalysts with disordered energy landscapes.[14–16] For instance, we have recently demonstrated that enhanced electron generation could be obtained in semicrystalline polymeric photocatalysts, in which effective exciton dissociation at order–disorder interfaces was identified, thus leading to excellent performance in charge-carrier-involved photocatalytic reactions.[16] As is well known, defects can significantly distort the distribution of electronic states in the system, which inspires us to consider their potential roles in exciton dissociation. In term of photocatalysis, defect engineering has been widely accepted as one of the most effective strategies that is closely related to absorption range, charge separation, transport properties, or active sites of catalysts,[17–21] whereas the relevant impacts on excitonic processes are far from being explored. To this end, we concentrate on bismuth oxyhalides, whose robust excitonic effects, easy structural modification, and promising photocatalytic activities[20,22–26] enable us to evaluate the impact of defective structures on the involved excitonic processes and the resulting photocatalytic performance.

Herein, by taking bismuth oxybromide (BiOBr) as a prototypical model system, we demonstrate for the first time that the incorporated oxygen vacancies (OV) can significantly accelerate exciton dissociation, giving rise to enhanced charge-carrier generation. Benefiting from the charge-carrier harvesting, the defective BiOBr with oxygen vacancies exhibits excellent performance in charge-carrier-involved photocatalytic reactions like superoxide generation and aerobic oxidative coupling of amines. This study provides an in-depth understanding on the design of advanced photocatalysts via defect engineering.

EXPERIMENTAL SECTION

Preparation of samples. Firstly, BiOBr nanoplates with (001) exposed facet were prepared by a modified hydrothermal method according to previous reports.[26] In detail, 2.425 g bismuth nitrate pentahydrate and 0.595 g potassium bromide were successively added into the mixture of 70 mL distilled water and 5 mL ethylene glycol under continuous stirring for 30 min. The mixed solution was then transferred into 100 mL Teflon lined autoclave and heated in a sealed autoclave at 160 °C for 24 hours. Upon being cooled to room temperature naturally, the precipitate was collected and washed with distilled water for several times, and then the products were dried under vacuum for 12 hours. After another heating treatment under high-purity O_2 atmosphere (0.5 MPa, 2 hours at 300 °C, to remove the tiny amount of oxygen vacancies), the powder sample (denoted BiOBr) was collected. The defective sample (denoted BiOBr-OV) was obtained through a heating treatment under vacuum condition (~10^{-3} Pa, 3 hours at 300 °C).

Calculations. First-principles calculations were performed by using the Vienna *ab* initio simulation package. The interactions between ions and valence electrons were described using the projector augmented wave potentials, and the generalized gradient approximation in the Perdew–Burke–Ernzerhof form was employed to correct the exchange correlations between electrons. The one-electron wave functions on a plane-wave basis were expanded with an energy cutoff of 500 eV. The Brillouin zones (with the *k*-point separation <0.05 $Å^{-1}$) for all the structures were sampled by using the Gamma-centered Monkhorst–Pack mesh. All of the atoms and geometries were allowed to relax and fully optimized, until the forces on atoms were less than 0.01 eV $Å^{-1}$. The energy cutoff for calculating the numbers of localized valence and conduction charge density near band-edge was set to 0.3 eV.

3,3',5,5'-tetramethylbenzidine (TMB) tests. In a typical test, 1 mg catalyst was dispersed into 2 mL TMB solution (500 μM, HAc/NaAc buffer solution), the mixture was illuminated after the saturation of adsorption by using a xenon lamp (PLS-SXE300/300UV, Trusttech Co., Ltd., Beijing) with a 420-nm cutoff filter as the light source. The oxidation of TMB molecules was evaluated by monitoring the absorbance change of the solution with a UV–vis spectrophotometer. The scavenger tests were performed as the above procedure with certain amounts of different scavengers, that is, carotene, 4 mg; mannite, 50 mM, 300 μL; catalase, 4000 unit/mL, 300 μL; superoxide dismutase (SOD), 4000 unit/mL, 300 μL.

ESR-trapping measurements. 50 μL of aqueous suspension of samples (4 g L^{-1}) was mixed with 500 μL of 2,2,6,6-tetramethylpiperidine (TEMP, 10 mM) solution. After being illuminated for 2 min, the mixture was characterized using a Bruker EMX plus model spectrometer operating at the X-band frequency (9.4 GHz) at room temperature. The $O_2^{\bullet-}$ and H_2O_2 trapping-ESR tests were performed in absolute methanol as described above, except using 5,5-dimethyl-1-pyrroline-*N*-oxide (DMPO, 20 mM) as the spin-trapping agent. A xenon lamp with a 420-nm cutoff filter was employed as the light source.

Characterizations. The X-ray diffraction (XRD) patterns were obtained on a Philips X'Pert Pro Super diffractometer with Cu *K*α radiation (λ = 1.54178 Å). The scanning electron microscopy (SEM) images were obtained on a JEOL JSM-6700F SEM. The high-angle annular dark-field scanning transmission electron microscopy (HAADF–STEM) measurement was carried out on a JEOL JEM-ARM200F microscope with spherical aberration correction. The X-ray photoelectron spectra (XPS) were collected on an ESCALAB MKII with Mg *K*α ($\hbar\nu$ = 1253.6 eV) as the excitation source, using C 1s (284.6 eV) as a reference. The valance band XPS spectra were collected at the catalysis and surface science endstation in the National Synchrotron Radiation Laboratory (NSRL), Hefei, China. The electron spin resonance (ESR) measurements were carried out on a Bruker EMX plus model spectrometer operating at the X-band frequency (9.4 GHz). The ultraviolet–visible (UV–vis) spectra were collected on a Perkin Elmer Lambda 950 UV–vis–NIR spectrophotometer. The Fourier transform infrared (FT-IR) spectra were recorded on a Magna-IR750 FT-IR spectrometer in a KBr pellet at room temperature. The NMR experiments were performed on a 400-MHz Bruker AVANCE AV III NMR spectrometer. The electrochemical measurements were carried out on an electrochemical workstation (CHI760E, Shanghai Chenhua Limited, China). The steady-state fluorescence and phosphorescence spectra as well as the time-resolved phosphorescence spectra were collected on a FLUOROLOG-3-TAU fluorescence spectrometer. The nanosecond-domain time-resolved fluorescence spectra were acquired on an FLS920 fluorescence spectrometer (Edinburgh Instruments Ltd.). The ultrafast transient absorption (TA) measurements were performed, under ambient conditions, on an ExciPro pump–probe spectrometer (CDP) coupled to an amplified femtosecond (fs) laser system (3 mJ, 35 fs; Coherent) with a temporal resolution of ~100 fs. The X-ray absorption spectra (XAS) were measured at the beamline BL12b of National Synchrotron Radiation Laboratory (NSRL, China) in the total electron yield mode by collecting the sample drain current under a vacuum better than 5×10^{-8} Pa.

RESULTS AND DISCUSSION

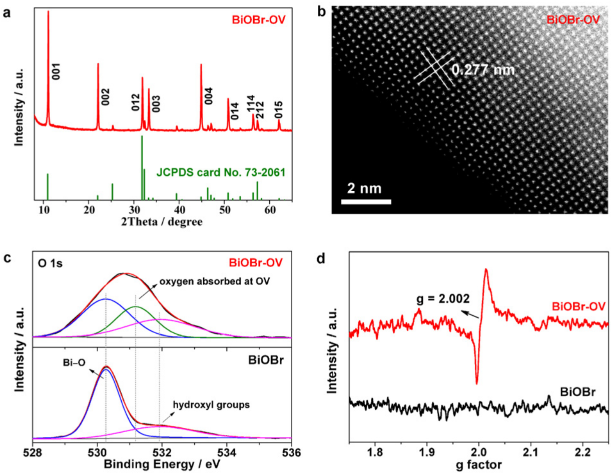

Figure 1. (a) XRD pattern and (b) atomic-resolution HAADF–STEM image of BiOBr-OV. (c) O 1s spectra and (d) room-temperature ESR spectra of both BiOBr-OV and BiOBr samples.

In this study, the BiOBr samples with and without oxygen vacancies (denoted BiOBr-OV and BiOBr, respectively) were prepared by an annealing treatment on the BiOBr nanoplates under vacuum and O_2 atmosphere, respectively. The structural investigation of both samples with the XRD patterns (Figure 1a and Figure S1) demonstrated the high purity with orientation along the [001] direction (JCPDS card No. 73-2061). The typical vibration modes revealed by Raman spectra (Figure S2) also confirmed the structural information of the samples, while the defective BiOBr-OV sample exhibits red-shifted bands with respect to the BiOBr sample, which can be assigned to the slight structural distortion induced by oxygen vacancies.[24] The SEM measurements (Figure S3) suggested a similar morphology for the two samples. Further atomic-resolution HAADF–STEM (Figure 1b) image revealed the single crystal feature of the sample, in which the atomic distance of ~0.277 nm was in accordance with the Bi atom arrangement of (001) facet. Given that the intensity of HAADF–STEM image is roughly proportional to the square of atomic number (namely, *Z*-contrast), the extremely large specific value of Z_{Bi}^2/ Z_O^2 (~107.6) makes it impossible to observe oxygen vacancy directly. The XPS results gave detailed information on chemical bonds of the samples. The XPS survey spectra revealed the chemical compositions (i.e., bismuth, oxygen, and bromine), indicating the high purity of the samples (Figure S4). As compared to BiOBr with two main components from lattice oxygen (530.3 eV) and hydroxyl groups (531.9 eV), the broadened O 1s spectrum (Figure 1c) with BiOBr-OV can be ascribed to the promoted contribution (531.2 eV) from the adsorbed oxygen species at the vacancy sites.[27,28] The Bi 4f spectrum of BiOBr (Figure S5) presents a typical spin–orbit doublet splitting centered at 159.7 and 165.0 eV. By comparison, the Bi 4f spectrum of BiOBr-OV exhibits an obvious 0.4-eV red-shift, which can be assigned to the breakage of Bi–O bond caused by oxygen vacancies. As one of the most effective techniques for probing defective structures, ESR spectroscopy was employed to glean more direct evidence. As displayed in Figure 1d, the BiOBr-OV sample turned out to possess an typical ESR signal centered at g = 2.002, owing to the electrons trapped on the oxygen vacancies. No obvious ESR signal was detected for the BiOBr case. As an effective technique for charactering local atomic environments, XAS was employed to verify the obvious change of hybridization strengths of Bi–O bonds induced by oxygen vacancies (Figure S6). The UV–vis spectra (Figure S7) revealed the similar absorption range and band gaps (~2.85 eV) for the two samples. Moreover, excitonic absorption in BiOBr system was observed in the high-resolution UV–vis spectra，showing weak absorption bands at 470 nm for both cases. It is worth noting that the oxygen vacancies in BiOBr-OV are mainly the bulk defects, rather than surface defects, in light of the similar nitrogen adsorption isotherms for the two samples (Figure S8).[23] According to the above characterizations and discussions, we can safely conclude that the BiOBr samples with oxygen vacancies have been successfully prepared.

It is widely accepted that defective structures would inevitably influence the electronic structure of materials. Herein, we conducted first-principles calculations based on density functional theory to investigate the impact of oxygen vacancy on the electronic structure of the BiOBr system. As shown in Figure S9, the calculated charge

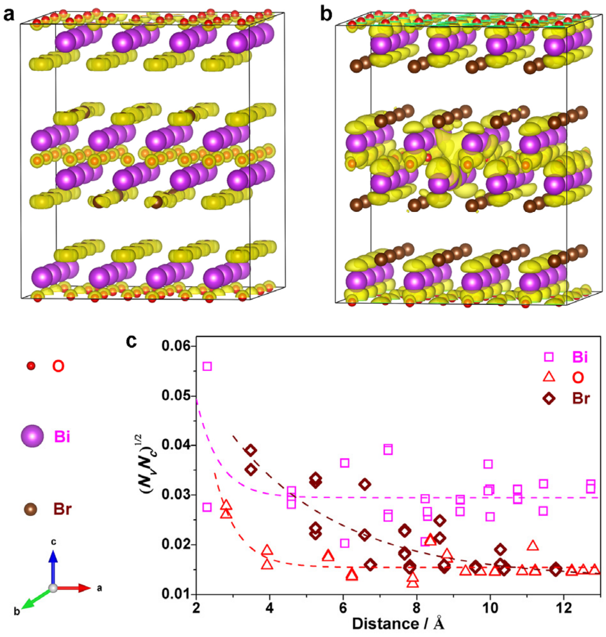

Figure 2. (a) Valence charge density and (b) conduction charge density near the band edges of BiOBr model with oxygen vacancy. (c) The $(N_cN_v)^{1/2}$ value of atomic sites at different distances around oxygen vacancy.

density of the defect energy level in BiOBr with oxygen vacancy suggested a strong localized charge density around the vacancy sites, leading to energetic disorder therein. Moreover, it turned out that oxygen vacancy tends to pose more impacts on the charge density distributions at the bromine sites, as seen from the obvious localized charge densities on the second- and third-nearest neighbor bromine sites. Given that the interacting holes and electrons (related to the excitonic effects) mainly originate from the states close to the valence band maximum and conduction band minimum, it is necessary to investigate the charge localization near the band edges in defective BiOBr.[26,29,30] As displayed in Figure 2a, the valence-band-edge charge density is mainly contributed by oxygen and bromine atoms, while oxygen vacancy shows an evident impact on the charge density localization of the nearby bromine atoms (within a distance of ~7 Å). In comparison, Figure 2b illustrates the disorder distribution of the conduction-band-edge charge density with a dominant contribution from the bismuth atoms. Note that the partial contributions from the nearby bromine atoms and the nearest oxygen atoms have also been verified. Given that the simultaneous localizations of conduction and valence band-edge states on Bi atomic sites are responsible for the significant electron–hole interaction, the disorder-redistributed band-edge states would greatly influence the stability of excitons near the vacancy sites. Herein, the products of the numbers of localized valence and conduction states near band edges for different atoms (denoted N_cN_v, where N_c and N_v are the numbers of localized conduction and valence states near band edges, respectively, within a cutoff energy) were calculated to elucidate the electron–hole interaction at certain atoms (Figure 2c). For the three kinds of atoms far away from the oxygen vacancies, the corresponding $(N_cN_v)^{1/2}$ values were found to keep constant, among which the bismuth atoms possess the largest $(N_cN_v)^{1/2}$ values, which revealed the significant, simultaneous localizations of conduction and valence band-edge states, in accordance with our previous report.[26] Nevertheless, the $(N_cN_v)^{1/2}$ values of the three kinds of atoms close to the vacancy sites exhibit distinctly different tendencies. As for the nearby bromine atoms (~10 Å), the $(N_cN_v)^{1/2}$ values obviously increase with decreasing the distances, suggesting enhanced electron–hole interaction at these atoms. By contrast, the $(N_cN_v)^{1/2}$ values for the oxygen and bismuth atoms show a negligible increase aside from the nearest neighboring sites. By virtue of the comparable $(N_cN_v)^{1/2}$ values for the three kinds of atoms, the extended (that is, delocalized) band-edge states can be expected, thus leading to the formation of much less compact excitons, which is less stable than the compact ones (Bi-case). In this case, it is rational to infer that excitons are unstable once they approach to the oxygen vacancies. It should be noted that the DFT results only gave a qualitative prediction of the trend in excitonic properties, rather than the kinetics of excitons.

On the basis of the above theoretical simulations, we propose that the event of exciton dissociation can be realized in the presence of oxygen vacancy. To verify this, we performed photoluminescence measurements under both ambient and low-temperature conditions. The prompt fluorescence spectra at 300 K recorded on the two samples are shown in Figure 3a. As for BiOBr-OV, the fluorescence spectrum exhibits two main peaks centered at 430 and 610 nm: the former can be assigned to the intrinsic band-edge emission (corresponding to the band gap of ~2.85 eV), while the latter is a characteristic emission from the defect state induced by oxygen vacancies.[23] In comparison, no obvious emissions were observed for BiOBr due to its indirect band feature. To further understand the photoexcitation processes involved in BiOBr-OV, we performed time-resolved prompt fluorescence measurements by monitoring the corresponding emission peaks. The results shown in Figure 3b indicated that the lifetimes of such emissions are both on a nanosecond timescale. Strikingly, the emission induced by oxygen vacancy exhibits a much longer lifetime (~19 ns) with respect to the intrinsic band-edge emission (~5 ns), suggesting distinctly different relaxation processes of the residential charge carriers in the two states.

The dark feature and the robust nonradiative relaxation of excitons urged us to pursue excitonic emissions under low temperatures.[31–33] As displayed in Figure 3c, the prompt fluorescence spectrum of BiOBr recorded at 8 K exhibits a strong sub-bandgap emission at around 482 nm, which can be attributed to the radiative decay of excitons.

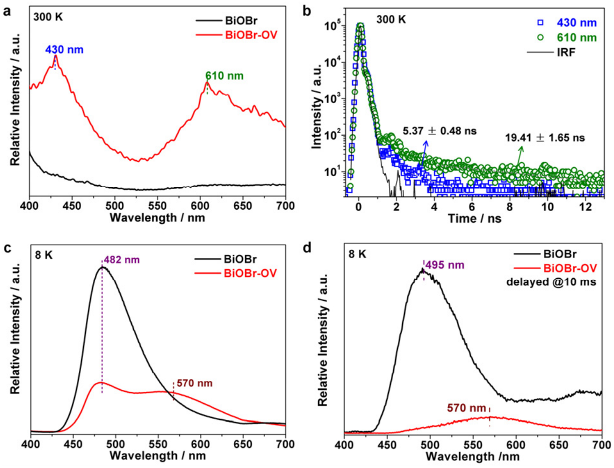

Figure 3. (a) Prompt fluorescence of BiOBr and BiOBr-OV samples under room temperature. (b) Time-resolved photoluminescence spectra of BiOBr-OV sample monitored at 430 and 610 nm. (c) Low temperature (8 K) prompt fluorescence and (d) low temperature steady-state phosphorescence recorded at a delayed time of 10 ms for both BiOBr and BiOBr-OV samples. All the photoluminescence spectra are recorded with a 380-nm excitation.

The slight red-shift in emission with respect to our previous report[26] is attributed to the different synthetic methods in the two works. However, apart from the excitonic emission, the BiOBr-OV sample exhibits another distinct emission peak at around 570 nm that can be associated with the oxygen vacancy states. Note that the blue-shift of oxygen-vacancy-induced emission from 610 to 570 nm arises as a result of the reduced electron–phonon interaction under low temperature.[34,35] In view of the spin-forbidden character of the excitonic emission, we further performed phosphorescence measurements on the samples (Figure 3d). With a long delayed time of 10 ms, the BiOBr sample exhibits a similar emission to the prompt one, expect for the red-shift from 482 to 495 nm. In contrast, the BiOBr-OV sample exhibits a dominant emission at around 570 nm, with negligible excitonic emission. The huge difference between the vacancy-state lifetime (~19 ns) and the delayed time (10 ms) suggested the strong correlation between the excitonic and defect emissions; in other words, the exciton dissociation at the oxygen-vacancy sites is responsible for the lasting defect emission. The time-resolved phosphorescence spectra (Figure S10) recorded at 495 and 570 nm for BiOBr and BiOBr-OV suggested the sub-second lifetimes for the emissions (~90.2 and 54.0 ms, respectively), of which the faster decay in BiOBr-OV also verified the promoted exciton relaxation induced by oxygen vacancy. Also, the high photocurrent response of BiOBr-OV echoed well to its promoted exciton dissociation and increased carrier concentrations (Figure S11), whereas the relatively low photocurrent response of BiOBr was in accordance with the robust excitonic effects of the system. The above results clearly demonstrated the oxygen-vacancy-induced exciton dissociation in BiOBr-OV.

To gain in-depth understanding on the influence of oxygen vacancy on excitonic processes, we further interrogated the BiOBr and BiOBr-OV samples with femtosecond time-resolved transient absorption (TA) spectroscopy, a robust tool for tracking in real time the relaxation kinetics of photogenerated charge carriers in semiconductor systems.[36–38] Herein, we chose a pump–probe configuration with a 380-nm pump and a white-light probe (430–610 nm) to trace the photogenerated electron kinetics. As shown in Figure 4a, similar TA spectral profiles (taken at a probe delay of 3 ps) manifested as photoinduced absorption (in positive values) were observed for both BiOBr and BiOBr-OV, in which the intensity difference can serve as an indicator of carrier concentration. Nevertheless, a pronounced difference in relaxation kinetics for the two cases was observed. Since it turned out that the TA kinetics were insensitive to the probing wavelength, we present in Figure 4b a representative set of data taken 550 nm. Clearly, the BiOBr-OV sample exhibits a much longer recovery lifetime of photoexcited electrons as compared to the BiOBr sample, which would facilitate the migration of charge carriers for photocatalytic reactions. As for BiOBr, the observed bi-exponential decay processes (τ_1 = 3.9 ± 0.5 ps, 74%; τ_2 = 81.8 ± 10.9 ps, 26%) suggested a consecutive, trap-state-mediated relaxation of the photogenerated electrons,[39,40] with an average lifetime of ~24 ps. Given the robust excitonic effects in the BiOBr system, the two consecutive relaxation pathways can be understood according to the scheme in Figure 4c (black dotted lines), where the excitonic state acts as an intermediate trap state (i.e., exciton-mediated trap state). Markedly, it turned out that the TA kinetics of BiOBr-OV can only be fitted well by a tri-exponential decay function (τ_1 = 4.4 ± 0.2 ps, 51%; τ_2 = 53.0 ± 4.2 ps, 21%; τ_3 = 944.7 ± 50.1 ps, 28%; average lifetime ~278 ps), rather than a bi-exponential decay function. By combining the TA analyses with the information from the above photoluminescence results, we schematically illustrate the three-step relaxation pathways in Figure 4c by the olive solid lines. After the photoexcited electrons undergo a fast relaxation (τ_1, a few picoseconds) from the conduction band minimum to the exciton-mediated trap state, the resulting excitons would then relax to the oxygen-vacancy-mediated trap state and meanwhile dissociate into free carriers (τ_2, a few tens of picoseconds), and eventually decay on a nanosecond timescale (τ_3). The above assignments were based on the following facts: the first component of BiOBr-OV (~4.4 ps) nicely matches the corresponding value of BiOBr (~3.9 ps); the second relaxation in BiOBr-OV (~53 ps) is faster than the exciton decay in BiOBr (~81.8 ps); the third component (~0.9 ns) in the TA probing time window is in agreement with the nanosecond-level lifetime of the oxygen-vacancy-induced fluorescence. It is worth noting that the photophysical processes in Figure 4c only illustrated the relaxation of electrons (with the energy position of the trap states being schematically depicted; see detailed information of the band structures in Figure S12). Therefore, the ultrafast TA analyses further highlighted the role of the oxygen-

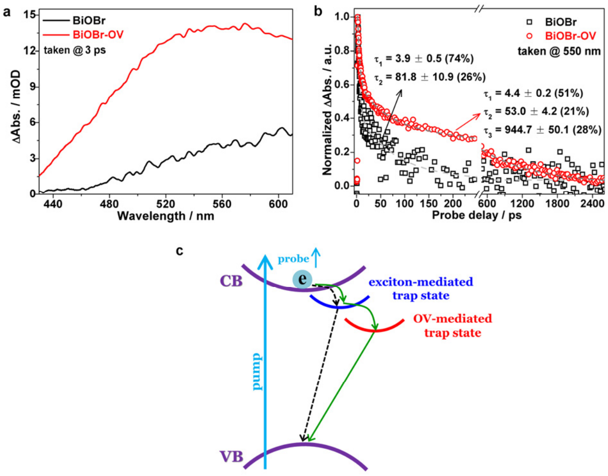

Figure 4. (a) Representative TA spectra taken at the probe delay of 3 ps for both samples. (b) TA kinetic traces probed at 550 nm for both samples. (c) Schematic illustration of the photophysical processes involving exciton- and oxygen-vacancy-mediated trap states.

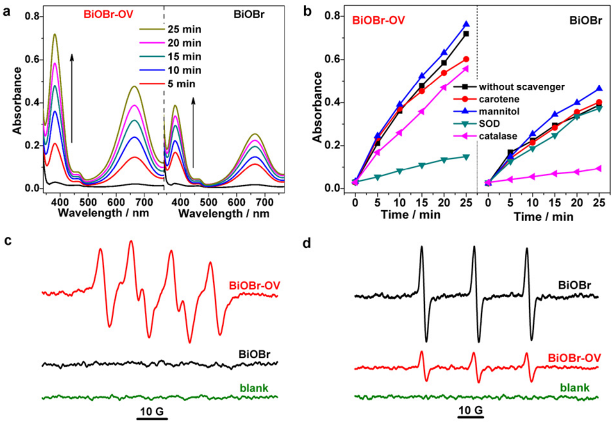

Figure 5. (a) Time-dependent absorption spectra of TMB oxidation with BiOBr and BiOBr-OV in air. (b) The absorbance evolution of TMB oxidation with BiOBr and BiOBr-OV monitored at the peak around 380 nm in the presence of different scavengers. (c) ESR spectra of different samples in the presence of DMPO in methanol. (d) ESR spectra of different samples in the presence of TEMP in water.

vacancy-induced exciton dissociation and the involved photoinduced processes in the BiOBr system.

On the basis of the boosted exciton dissociation and charge-carrier generation, one can expect a promoted charge-carrier-involved photocatalytic activity with the defective BiOBr sample. Herein, we carried out molecular oxygen activation measurements to evaluate the involved photocatalytic performance under visible-light illumination ($\lambda \geq 420$ nm). 3,3',5,5'-tetramethylbenzidine (TMB) was selected as the probe molecule, by monitoring the absorbance change of the solution. The absorption evolution of TMB solutions (Figure 5a) clearly suggested the generation of reactive oxygen species (ROS) for both samples. Obviously, the BiOBr-OV sample exhibits promoted molecular oxygen activation ability. The scavenger measurements were further performed to identify the functional ROS in the two cases, where superoxide dismutase (SOD), mannitol, catalase, and carotene were used to selectively eliminate superoxide ($O_2^{\bullet-}$), hydroxyl radicals (•OH), hydrogen peroxide (H_2O_2), and singlet oxygen ($^1O_2$), respectively. As shown in Figure 5b, significant suppression of TMB oxidation was observed in the presence of SOD, whereas the other scavengers were found to execute much less influence on TMB oxidation. Therefore, $O_2^{\bullet-}$ can be determined to be the dominating ROS in the photocatalytic molecular oxygen activation of BiOBr-OV. On the other hand, $^1O_2$ mainly accounts for TMB oxidation in the BiOBr case, pointing to its giant exciton effects. ESR measurement, which can provide one of the most convictive evidences to identify the ROS products, was further performed to verify the different photocatalytic ROS generation in the two cases. Here, 5,5-dimethyl-1-pyrroline-*N*-oxide (DMPO) was selected as the trapping agent for the detection of $O_2^{\bullet-}$ in methanol. The strong, sextet ESR signal for BiOBr-OV case displayed in Figure 5c verified the formation of DMPO–OOH, which is a spin adduct derived from DMPO–$O_2^{\bullet-}$, thus offering conclusive evidence for the promoted generation of $O_2^{\bullet-}$. In contrast, the BiOBr sample led to negligible $O_2^{\bullet-}$ production. On the other hand, the $^1O_2$ generation was verified by using 2,2,6,6-tetramethylpiperidine (TEMP) as the trapping reagent. As shown in Figure 5d, the typical 1:1:1 triplet signal with g-value of 2.0056 for BiOBr is in good agreement with those of 2,2,6,6-tetramethylpiperidine-*N*-oxyl (TEMPO), confirming its high $^1O_2$ generation. In comparison, a tiny TEMPO signal was observed in the BiOBr-OV case, demonstrating the significant suppression in $^1O_2$ generation. Moreover, negligible H_2O_2 generation was detected under visible-light illumination in both cases (Figure S13). Besides, the $O_2^{\bullet-}$ generation was demonstrated to be dependent on the concentration of oxygen vacancies, verifying the defect-mediated exciton dissociation in BiOBr system (Figure S14). The influence of different light absorption and potential hydrogen incorporation in the two samples were also investigated, showing negligible impacts on the ROS generation (Figure S15 and S16). On the basis of the above measurements, we conclude that the existence of oxygen vacancies greatly facilitates the charge-carrier-involved photocatalytic ROS generation in the BiOBr system.

The conversely generated $O_2^{\bullet-}$ and $^1O_2$ yields suggested the totally different photoexcitation processes induced by oxygen vacancy. Generally, $^1O_2$ generation is believed to undergo an energy transfer process between ground-state molecular oxygen and long-lived excitons,[41,42] while $O_2^{\bullet-}$ generation mainly involves photogenerated electron transfer between molecular oxygen and catalysts. The possible charge transfer process for $^1O_2$ generation in BiOBr was excluded by scavenger tests (Figure S17). In this case, it is reasonable for the detection of high $^1O_2$ but negligible $O_2^{\bullet-}$ in the presence of BiOBr, whose confined layered structure sustains a considerable exciton binding energy. The large exciton binding energy implies strong correlations between photogenerated holes and electrons, thus giving rise to high exciton concentration but low electron yield. As for the defective case, the tiny $^1O_2$ generation suggested the significantly suppressed excitonic processes, while a much higher $O_2^{\bullet-}$ yield indicated the promoted electron concentration in BiOBr-OV with respect to BiOBr. The intriguing, complementary evolutions of $^1O_2$ and $O_2^{\bullet-}$ in BiOBr-OV further confirmed the positive role of oxygen vacancy on exciton dissociation into free charge carriers.

Table 1. Aerobic oxidative coupling of amines.[a]

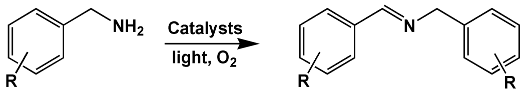

Entry	R	Time / h	BiOBr		BiOBr-OV	
			Conv.[b]	Select.[c]	Conv.	Select.
1	H	12	24	95	96	99
2[d]	H	12	9	trace	5	trace
3[e]	H	12	35	27	17	trace
4	*p*-F	8	31	90	99	99
5	*p*-Cl	8	24	95	99	99
6	*p*-Me	15	49	94	94	95
7	*p*-OMe	24	34	97	56	90
8	*o*-Cl	8	27	99	99	99
9	*m*-Cl	8	36	97	99	99
10	*o*-Me	15	56	95	99	96
11	*m*-Me	15	42	95	99	95

[a] Reaction conditions: substrate (0.2 mmol), catalyst (10 mg), acetonitrile (1 ml), air, 20 °C, xenon lamp with a cut-off filter ($\lambda \geq$ 420 nm). [b] Determined by NMR analyses, using *s*-trioxane as the internal standard, mol%. [c] Selectivity = $\text{yield}_{\text{imine}}*2$ / $\text{conversion}_{\text{amine}}$, mol%. [d] Argon atmosphere. [e] Additional methanol 100 μL.

By virtue of its high-efficiency $O_2^{\bullet-}$ generation, the defective BiOBr-OV sample can be expected to hold great potential in photocatalytic organic syntheses. Herein, aerobic oxidative coupling of amines to imines, which is an extensively studied reaction due to its critical role in the fields of chemistry and biology,[43,44] was employed to evaluate the photocatalytic performance of the defective sample (Figure S18). Herein, a series of amines were selected as the oxidation substrates, of which the conversion rates and selectivities under the optimized conditions are listed in Table 1. In detail, the defective sample can convert benzylamine (entry 1; Figure S19) to *N*-benzylidenebenzylamine with high efficiency and selectivity, while the yield of corresponding imine was much lower in the BiOBr case. The high selectivity in the BiOBr case is ascribed to the $^1O_2$-involved mechanism for the oxidative coupling of benzylamines,[45] whereas the low conversion rate may originate from the exciton–exciton annihilation induced, relatively inefficient quantum yields. To verify the vital role of ROS on the reaction, control groups under inert atmosphere were examined, where the conversion yields were significantly suppressed for both BiOBr and BiOBr-OV (entry 2). Besides, the additional methanol (an effective hole-scavenger, entry 3) significantly suppressed the conversion rate and selectivity for BiOBr-OV case, in accordance with the formation of cation radical complex through the hole-oxidation within the $O_2^{\bullet-}$-involved mechanism (as illustrated in Figure S18),[46] whereas the incomplete suppression for BiOBr case could be related to the $^1O_2$-involved mechanism. We further looked into the influence of substituent groups on the oxidative-coupling reaction. The results suggested that the defective sample possesses much higher yields than the BiOBr sample for both electron-withdraw (*para*-F, entry 3; *para*-Cl, entry 4) and electron-donating (*para*-CH_3O, entry 5; *para*-CH_3, entry 6) cases, which confirmed the dominating advantage arising from the oxygen-vacancy-induced exciton dissociation in BiOBr-OV. Moreover, as compared with the electron-donating cases, the electron-withdraw groups exhibited positive roles in these oxidative coupling reactions (refer to the much higher reaction rates), echoing well to the $O_2^{\bullet-}$-involved mechanism in the BiOBr-OV case. The factor of substitution position in benzylamine derivatives was also investigated, which exhibited negligible impact on the yields of corresponding imines (*ortho*-Cl, entry 7; *meta*-Cl, entry 8; *ortho*-CH_3, entry 9; *meta*-CH_3, entry 10). The cycling tests of oxidative coupling of benzylamines (Figure S20) were further performed, which exhibited negligible reduction within five consecutive cycles, verifying the excellent photocatalytic stability of the BiOBr-OV samples. The above results confirmed the outstanding performance of the BiOBr-OV system for selective oxidation, opening an intriguing prospective in further applications.

CONCLUSION

In conclusion, we have systematically investigated the influence of oxygen vacancy on photoinduced processes in a prototypical model of BiOBr, where the oxygen-vacancy-mediated exciton dissociation in the catalyst was highlighted for the first time. Theoretical simulations suggested that oxygen vacancy (OV) can significantly distort the localization of the band-edge states around the defective sites, leading to instability of excitons. By the joint observations from photoluminescence spectroscopy and photoelectrochemical experiments, we demonstrated the oxygen-vacancy-mediated exciton dissociation that results in promoted charge-carrier generation in the system. Such an effect was further verified by ultrafast transient absorption spectroscopy, establishing an in-depth understanding on the pertinent photophysical processes. Benefiting from the robust exciton dissociation, the defective BiOBr-OV system was demonstrated to exhibit excellent performance in charge-carrier-involved photocatalytic reactions such as superoxide radical generation and selective oxidative-coupling reaction. This work not only sheds new light on the photoinduced processes of the well-established catalysts, but also provides a defect-engineering strategy on excitonic regulation.

ASSOCIATED CONTENT

Supporting Information. This material is available free of charge via the Internet at http://pubs.acs.org.

Additional structural characterizations; theoretical calculations; photoluminescence spectra;

photoelectrochemical tests; and photocatalytic measurements (PDF)

AUTHOR INFORMATION

Corresponding Author

zhxid@ustc.edu.cn; qunzh@ustc.edu.cn; yxie@ustc.edu.cn

Author Contributions

‡ These authors contributed equally.

Notes

The authors declare no competing financial interest.

ACKNOWLEDGMENT

The work was supported by the National Key R & D Program on Nano Science & Technology of the MOST (2017YFA0207301, 2016YFA0200602), the National Natural Science Foundation of China (U1532265, U1632149, 11621063, 21401181, 21573211, 21633007), the Youth Innovation Promotion Association of CAS (2017493), Anhui Provincial Natural Science Foundation (1708085QB24), Key Research Program of Frontier Sciences (QYZDY-SSW-SLH011), the National Postdoctoral Program for Innovative Talents (BX201700219), and the Fundamental Research Funds for the Central Universities (WK2340000063). The authors thank Dr. Huanxin Ju (National Synchrotron Radiation Laboratory, USTC) for his helpful suggestions on the valance band XPS analyses.

REFERENCES

(1) Congreve, D.; Lee, J.; Thompson, N.; Hontz, E.; Yost, S.; Reusswig, P.; Bahlke, M.; Reineke, S.; Van Voorhis, T.; Baldo, M. *Science* **2013**, *340*, 334. 1. Hoffmann, M.; Martin, S.; Choi, W.; Bahnemann, D. *Chem. Rev.* **1995**, *95*, 69.

(2) Chen, C.; Ma, W.; Zhao, J. *Chem. Soc. Rev.* **2010**, *39*, 4206.

(3) Chen, X.; Shen, S.; Guo, L.; Mao, S. *Chem. Rev.* **2010**, *110*, 6503.

(4) Serpone, N.; Emeline, A. *J. Phys. Chem. Lett.* **2012**, *3*, 673.

(5) Tian, Y.; Tatsuma, T. *J. Am. Chem. Soc.* **2005**, *127*, 7632.

(6) Mangold, M.; Weiss, C.; Calame, M.; Holleitner, A. *Appl. Phys. Lett.* **2009**, *94*, 161104.

(7) Marschall, R. *Adv. Funct. Mater.* **2014**, *24*, 2421

(8) Mongin, C.; Garakyaraghi, S.; Razgoniaeva, N.; Zamkov, M.; Castellano, F. *Science* **2016**, *351*, 369.

(9) Linsebigler, A.; Lu, G.; Yates, J. *Chem. Rev.* **1995**, *95*, 735.

(10) Wang, H.; Jiang, S.; Chen, S.; Li, D.; Zhang, X.; Shao, W.; Sun, X.; Xie, J.; Zhao, Z.; Zhang, Q.; Tian, Y.; Xie, Y. *Adv. Mater.* **2016**, *28*, 6940.

(11) Ma, Y.; Valkunas, L.; Dexheimer, S.; Bachilo, S.; Fleming, G. *Phys. Rev. Lett.* **2005**, *94*, 157402.

(12) Hendry, E.; Schins, J.; Candeias, L.; Siebbeles, L.; Bonn, M. *Phys. Rev. Lett.* **2004**, *92*, 196601.

(13) Wang, H.; Jiang, S.; Chen, S.; Zhang, X.; Shao, W.; Sun, X.; Zhao, Z.; Zhang, Q.; Luo, Y.; Xie, Y. *Chem. Sci.* **2017**, *8*, 4087.

(14) Paquin, F.; Latini, G.; Sakowicz, M.; Karsenti, P.; Wang, L.; Beljonne, D.; Stingelin, N.; Silva, C. *Phys. Rev. Lett.* **2011**, *106*, 197401.

(15) Paquin, F.; Rivnay, J.; Salleo, A.; Stingelin, N.; Silva-Acuña, C. *J. Mater. Chem. C* **2015**, *3*, 10715.

(16) Wang, H.; Sun, X.; Li, D.; Zhang, X.; Chen, S.; Shao, W.; Tian, Y.; Xie, Y. *J. Am. Chem. Soc.* **2017**, *139*, 2468.

(17) Chen, X.; Liu, L.; Yu, P.; Mao, S. *Science* **2011**, *33*, 746.

(18) Nowotny, M.; Sheppard, L.; Bak, T.; Nowotny, J. *J. Phys. Chem. C* **2008**, *112*, 5275.

(19) Ida, S.; Kim, N.; Ertekin, E.; Takenaka, S.; Ishihara, T. *J. Am. Chem. Soc.* **2015**, *137*, 239.

(20) Guan, M.; Xiao, C.; Zhang, J.; Fan, S.; An, R.; Cheng, Q.; Xie, J.; Zhou, M.; Ye, B.; Xie, Y. *J. Am. Chem. Soc.* **2013**, *135*, 10411.

(21) Wang, S.; Pan, L.; Song, J.; Mi, W.; Zou, J. J.; Wang, L.; Zhang, X. *J. Am. Chem. Soc.* **2015**, *137*, 2975.

(22) Li, J.; Yu, Y.; Zhang, L. *Nanoscale* **2014**, *6*, 8473.

(23) Li, H.; Shang, J.; Ai, Z.; Zhang, L. *J. Am. Chem. Soc.* **2015**, *137*, 6393.

(24) Wang, X.; Zhao, Y.; Li, F.; Dou, L.; Li, Y.; Zhao, J.; Hao, Y. *Sci. Rep.* **2016**, *6*, 24918.

(25) Li, H.; Li, J.; Ai, Z.; Jia, F.; Zhang, L. *Angew. Chem., Int. Ed* **2017**, doi:10.1002/anie.201705628

(26) Wang, H.; Chen, S.; Yong, D.; Zhang, X.; Li, S.; Shao, W.; Sun, X.; Pan, B.; Xie, Y. *J. Am. Chem. Soc.* **2017**, *139*, 4737.

(27) Uhlenbrock, S.; Scharfschwerdt, C.; Neumann, M.; Illing, G.; Freund, H. *J. Phys.: Condens. Matter* **1992**, *4*, 7973.

(28) Wang, L.; Ma, Y.; Wang, Y.; Liu, S.; Denng, Y. *Catal. Commun.* **2011**, *12*, 1458.

(29) Dvorak, M.; Wei, S. H.; Wu, Z. *Phys. Rev. Lett.* **2013**, *110*, 016402.

(30) Su, Y. Q.; Zhu, Y.; Yong, D. Y.; Chen, M. M.; Su, L. X.; Chen, A. Q.; Wu, Y. Y.; Pan, B. C.; Tang, Z. K. *J. Phys. Chem. Lett.* **2016**, *7*, 1484.

(31) Mortimer, I. B.; Nicholas, R. J. *Phys. Rev. Lett.* **2007**, *98*, 27404.

(32) Yersin, H. *Top. Curr. Chem.* **2004**, *241*, 1.

(33) Zhao, H.; Mazumdar, S. *Phys. Rev. Lett.* **2004**, *93*, 157402.

(34) Karaiskaj, D.; Engtrakul, C.; McDonald, T.; Heben, M. J.; Mascarenhas, A. *Phys. Rev. Lett.* **2006**, *96*, 106805.

(35) Karaiskaj, D.; Mascarenhas, A. *Phys. Rev. B* **2007**, *75*, 115426.

(36) Hong, X. P.; Kim, J.; Shi, S. F.; Zhang, Y.; Jin, C. H.; Sun, Y. H.; Tongay, S.; Wu, J. Q.; Zhang, Y. F.; Wang, F. *Nat. Nanotechnol.* **2014**, *9*, 682.

(37) Zhu, H.; Yang, Y.; Wu, K.; Lian, T. *Annu. Rev. Phys. Chem.* **2016**, *67*, 259.

(38) Zhang, Q.; Luo, Y. *High Power Laser Sci. Eng.* **2016**, *4*, e22.

(39) Bi, W.; Li, X.; Zhang, L.; Jin, T.; Zhang, L.; Zhang, Q.; Luo, Y.; Wu, C.; Xie, Y. *Nat. Commun.* **2015**, *6*, 8647.

(40) Yang, W.; Zhang, L.; Xie, J.; Zhang, X.; Liu, Q.; Yao, T.; Wei, S.; Zhang, Q.; Xie, Y. *Angew. Chem., Int. Ed.* **2016**, *55*, 6716.

(41) Kovalev, D.; Fujii, M. *Adv. Mater.* **2005**, *17*, 2531.

(42) Schweitzer, C.; Schmidt, R. *Chem. Rev.* **2003**, *103*, 1685.

(43) Jiang, G.; Chen, J.; Huang, J.; Che, C. *Org. Lett.* **2009**, *11*, 4568.

(44) Zhang, N.; Li, X.; Ye, H.; Chen, S.; Ju, H.; Liu, D.; Lin, Y.; Ye, W.; Wang, C.; Xu, Q.; Zhu, J.; Song, L.; Jiang, J.; Xiong, Y. *J. Am. Chem. Soc.* **2016**, *138*, 8928.

(45) Ushakov, D. B.; Gilmore, K.; Kopetzki, D.; McQuade, D. T.; Seeberger, P. H. *Angew. Chem., Int. Ed.* **2014**, *53*, 557.

(46) Su, C.; Acik, M.; Takai, K.; Lu, J.; Hao, S.-j.; Zheng, Y.; Wu, P.; Bao, Q.; Enoki, T.; Chabal, Y. J.; Ping Loh, K. *Nat. Commun.* **2012**, *3*, 1298.

Table of Contents